

# Determination of electron orbital magnetic moments in carbon nanotubes

E. D. Minot\*, Yuval Yaish\*, Vera Sazonova & Paul L. McEuen

Laboratory of Atomic and Solid-State Physics, Cornell University, Ithaca, New York 14853, USA

\* These authors contributed equally to this work

The remarkable transport properties of carbon nanotubes (CNTs) are determined by their unusual electronic structure<sup>1</sup>. The electronic states of a carbon nanotube form one-dimensional electron and hole sub-bands, which, in general, are separated by an energy gap<sup>2,3</sup>. States near the energy gap are predicted<sup>4,5</sup> to have an orbital magnetic moment,  $\mu_{\text{orb}}$ , that is much larger than the Bohr magneton (the magnetic moment of an electron due to its spin). This large moment is due to the motion of electrons around the circumference of the nanotube, and is thought to play a role in the magnetic susceptibility of CNTs<sup>6-9</sup> and the magnetoresistance observed in large multiwalled CNTs<sup>10-12</sup>. But the coupling between magnetic field and the electronic states of individual nanotubes remains to be quantified experimentally. Here we report electrical measurements of relatively small diameter (2–5 nm) individual CNTs in the presence of an axial magnetic field. We observe field-induced energy shifts of electronic states and the associated changes in sub-band structure, which enable us to confirm quantitatively the predicted values for  $\mu_{\text{orb}}$ .

The electronic structure of a CNT is elegantly described by the quantization of wave states around a graphene cylinder<sup>1</sup>. Graphene is a zero-bandgap semiconductor in which the valence and conduction states meet at two points in  $k$ -space,  $\mathbf{K}_1$  and  $\mathbf{K}_2$  (Fig. 1a). The dispersion around each of these points is a cone (Fig. 1b). When graphene is wrapped into a cylinder the electron wavenumber perpendicular to the CNT axis,  $k_{\perp}$ , is quantized, satisfying the boundary condition  $\pi D k_{\perp} = 2\pi j$  where  $D$  is the CNT diameter and  $j$  is an integer. The resulting allowed values of  $\mathbf{k}$  correspond to the horizontal lines in Fig. 1a that miss  $\mathbf{K}_i$  by an amount  $\Delta k_{\perp}$ . The conic

sections of the dispersion cones by allowed  $\mathbf{k}$  determine the CNT band structure near the Fermi level as shown in Fig. 1b. The upper and lower branches of the conic sections correspond to the conduction and valence states of the CNT. Both the  $\mathbf{K}_1$  and  $\mathbf{K}_2$  sub-bands have the same energy gap between conduction and valence states:  $E_g^0 = \hbar v_F \Delta k_{\perp}$ .

The size of  $\Delta k_{\perp}$ , and therefore  $E_g^0$ , depends on the CNT chirality<sup>1-3</sup> and perturbations such as curvature<sup>13</sup>, axial strain<sup>14,15</sup>, twist<sup>14</sup> and inner–outer shell interactions<sup>16</sup>. From consideration of chirality alone, CNTs are classified as metallic ( $\Delta k_{\perp} = 0$ ) or semiconducting ( $\Delta k_{\perp} = 2/3D$ )<sup>1</sup>. Perturbations displace the dispersion cones<sup>13</sup>, modifying  $\Delta k_{\perp}$  and resulting in an important class of small-bandgap ‘quasi-metallic’ CNTs<sup>17</sup>. We have used these small-bandgap CNTs in our measurements.

The electron states near the gap correspond to semiclassical electron orbits encircling the CNT. The perpendicular component of orbital velocity  $v_{\perp} = (1/\hbar) dE/dk_{\perp}$  determines the clockwise (CW) or anticlockwise (ACW) sense of an orbit. For example, in Fig. 1b we see that  $v_{\perp}$  is negative for the  $\mathbf{K}_1$  conduction states but is positive for  $\mathbf{K}_1$  valence states. By symmetry, each CW (ACW) orbit in the  $\mathbf{K}_1$  sub-band has an equal energy ACW (CW) partner in the  $\mathbf{K}_2$  sub-band. As a consequence, the two sub-bands are degenerate, but the CW/ACW sense of valence and conduction states is reversed.

From basic electromagnetic theory, an electron moving at velocity  $v$  around a loop of diameter  $D$  has an orbital magnetic moment of magnitude  $\mu = Dev/4$ . In a CNT, electron states at the bandgap edges, where  $v_{\perp}$  is largest, have an orbital magnetic moment of magnitude  $\mu_{\text{orb}} = Dev_F/4$  directed along the tube axis. A magnetic field parallel to the CNT axis,  $B_{\parallel}$ , is predicted to shift the energy of these states by:

$$\Delta E = -\mu_{\text{orb}} \cdot \mathbf{B} = \pm \frac{Dev_F B_{\parallel}}{4} \quad (1)$$

For CNTs with a finite energy gap at  $B_{\parallel} = 0$ , the energy gap of one sub-band becomes larger as  $B_{\parallel}$  is increased, while the energy gap of the other sub-band becomes smaller (Fig. 1c).

Previous work on the magnetoresistance of individual multiwalled nanotubes<sup>10-12</sup> and the magnetic susceptibility of CNT mats<sup>6,7</sup> has not confirmed the magnitude of  $\mu_{\text{orb}}$  or the splitting of sub-band degeneracy. In the current work we use two different techniques to achieve this goal: (1) thermally activated transport through individual small-bandgap CNTs that are depleted of charge

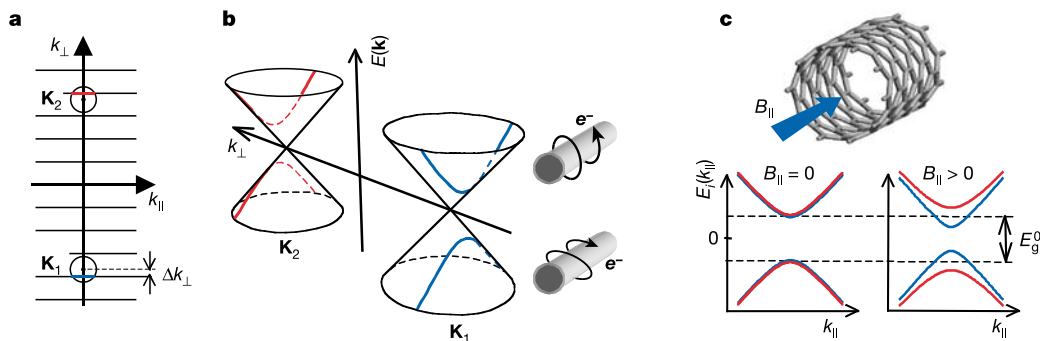


**Figure 1** Nanotube states near the bandgap and orbital magnetic moments. **a**, The valence and conduction states of graphene meet at  $\mathbf{K}_1$  and  $\mathbf{K}_2$ . Horizontal lines show the quantized values of  $k_{\perp}$  for the CNT structure in **c**. The misalignment between horizontal lines and the  $\mathbf{K}$ -points is  $\Delta k_{\perp}$ . **b**, Graphene dispersion near the  $\mathbf{K}$ -points is described by the cones  $E_i(\mathbf{k}) = \pm \hbar v_F |\mathbf{k} - \mathbf{K}_i|$ , with  $v_F = 8 \times 10^5 \text{ m s}^{-1}$  (ref. 1). Lines of allowed  $\mathbf{k}$  intersect the two cones (blue and red curves). The conduction states near  $\mathbf{K}_1$  (upper blue curve) have  $dE/dk_{\perp} < 0$ . Electrons in these states move around the CNT in an anticlockwise (ACW) fashion. The valence states near  $\mathbf{K}_1$  (lower

blue curve) have  $dE/dk_{\perp} > 0$  and are associated with clockwise (CW) electron motion. ACW (CW) orbits correspond to positive (negative) magnetic moments along the CNT axis. The conic section near  $\mathbf{K}_2$  lies on the opposite face of an identical dispersion cone. Therefore,  $\mathbf{K}_2$  conduction (valence) states have CW (ACW) orbits. **c**, Top, perspective view of a CNT in the presence of a magnetic field  $B_{\parallel}$ . Below, the dispersion relations  $E_1(k_{\parallel})$  and  $E_2(k_{\parallel})$ , shown in blue and red respectively. The sub-bands are degenerate at  $B_{\parallel} = 0$ . The magnetic field breaks this degeneracy.

carriers, (2) energy level spectroscopy near the bandgap edge of CNT quantum dots.

We have found that a suspended CNT device geometry (Fig. 2) is well suited for studying small changes in bandgap. Measurements of many such devices, using a gold-coated atomic force microscope (AFM) tip as a movable, local electrode<sup>18,19</sup>, show that CNT segments contacting the oxide substrate are doped p-type, while suspended sections of the same tube are almost intrinsic. At small gate voltage  $V_g$  the suspended section is depleted of charge carriers. The oxide-bound sections, however, remain p-doped and act as electrodes to the suspended section. By studying the conductance of the suspended section at different temperatures and magnetic fields we can determine changes in  $E_g^{K_i}$ .

Figure 3a shows device conductance  $G$  versus  $V_g$  of two small-bandgap CNTs. Device 1 shows a sharp dip near  $V_g = 0.4$  V, corresponding to depletion of carriers in the suspended segment. A second, broader dip occurs at  $V_g \approx 2$  V as the oxide-bound segments become depleted. The inset shows the dip from the suspended section of device 2. In both cases, the addition of a magnetic field substantially increases the conductance at the bottom of the dip.

When the suspended CNT segment is depleted, conductance occurs via thermal activation of carriers across the energy gap. Conductance is smallest at  $V_g = V^*$ , immediately before the suspended segment becomes n-type (Fig. 2c). The minimum conductance due to thermal activation,  $G_{act}(V^*)$ , can be estimated by considering the Fermi-Dirac function at temperature  $T$  and the Landauer formalism for one-dimensional (1D) conduction channels<sup>15,20</sup>

$$G_{act}(V^*, T) = \frac{2e^2}{h} \sum_{i=1,2} |t_i|^2 \frac{2}{\exp(E_g^{K_i}/k_B T) + 1} \quad (2)$$

where  $|t_i|^2$  is the transmission probability for thermally activated carriers in the  $i$ th sub-band. The device conductance  $G$  is a combination of  $G_{act}$  in series with the conductance of the p-type sections of CNT and the conductance of the metal–CNT contacts, both of which are largely temperature independent.

We have measured  $G$  versus  $V_g$  for devices 1 and 2 at several temperatures. In Fig. 3b (open circles) we plot the change in resistance  $\Delta R(T) = G(V^*, T)^{-1} - G(V_g \ll 0, T)^{-1}$  of device 2 at  $B = 0$  T. From the slope and intercept of the fitting exponential, and assuming sub-band degeneracy ( $E_g^{K_i} = E_g^0$ ) we find:  $E_g^0 = 40$  meV and  $|t_1|^2 + |t_2|^2 = 1.6$ . Because  $|t_1|^2 + |t_2|^2$  is close to 2, we conclude that transport is nearly ballistic and that both the  $K_1$  and  $K_2$  sub-bands make comparable contributions to the device conductance. We find similar values of  $E_g^0$  in both devices (see Table 1) even though the CNT diameters are significantly different. Further work is needed to identify the perturbations responsible for  $E_g^0$ .

Magnetic fields dramatically reduce  $\Delta R$ , as shown in Fig. 3c. The temperature dependence of  $\Delta R$  at  $B = 10$  T is also shown for device 2 (Fig. 3b, filled triangles). If we fit this high-field temperature data with the same method used for zero-field data, we find  $E_g^0 = 22$  meV and  $|t_1|^2 + |t_2|^2 = 0.8$ . The bandgap of at least one sub-band is significantly lowered by the magnetic field and we argue below that

the apparent change in  $|t_1|^2 + |t_2|^2$  is due to the increasing bandgap of the second sub-band.

The magnetic field dependence of  $\Delta R$  can be quantitatively described by equal and opposite changes in  $E_g^{K_1}$  and  $E_g^{K_2}$  owing to the coupling of  $\mu_{orb}$  with  $B_{\parallel}$ . We have accurately fitted our measurements of  $\Delta R(B, T)$  using equation (2) and setting  $E_g^{K_1} = E_g^0 - aB$  and  $E_g^{K_2} = E_g^0 + aB$  (see the fitted curves in Fig. 3c). The only fitting parameter is  $a$ ;  $E_g^0$  and  $|t_i|^2$  are found from the temperature dependence of  $\Delta R$  at  $B = 0$  T and setting  $|t_1|^2 = |t_2|^2$ .

The fitting results for devices 1 and 2 are summarized in Table 1. In agreement with equation (1), the measured  $\mu_{orb}$  scale with diameter and are an order of magnitude larger than previously measured spin magnetic moments in CNTs<sup>21,22</sup>. Thermally activated transport (equation (2)), combined with the breaking of CW/ACW sub-band degeneracy, describes  $\Delta R$  over a wide range of  $T$  and  $B$ . At  $B = 10$  T device conductance is almost entirely due to carriers that are thermally activated across the smaller bandgap. Transport occurs in a single sub-band, explaining why  $|t_1|^2 + |t_2|^2$  decreases by a factor of 2 when sub-band degeneracy is incorrectly assumed at high field. Our measurements confirm theoretical predictions<sup>4,5</sup> for the sign and magnitude of orbital magnetic moments in CNTs and show that an applied magnetic field can split the degeneracy of the  $K_1$  and  $K_2$  sub-bands.

Orbital magnetic moments should also influence the energy level spectra of CNT quantum dots (CNTQDs) in applied magnetic fields. In our device geometry a CNTQD forms when  $V_g > V^*$  and electrons are confined to conduction states of the suspended section by p–n tunnel barriers (Fig. 2c). Figure 4a shows the formation of a

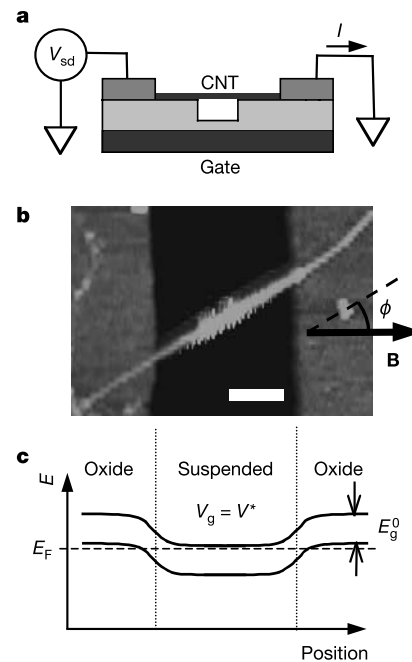


**Figure 2** Device geometry and band bending. **a**, CNTs are grown on Si/SiO<sub>x</sub> substrates by the chemical vapour deposition method<sup>26</sup>. Electrodes (5 nm Cr, 50 nm Au) are patterned by photolithography<sup>27</sup>. The central region of the CNT is suspended over a trench defined by electron-beam lithography and wet etching using 6:1 buffered HF. **b**, AFM image of the suspended section of CNT and nearby oxide-bound sections of device 1. Scale bar, 130 nm. The suspended section appears fuzzy because it is displaced by the AFM tip during imaging. From the image we find CNT diameter  $D = 2.6$  nm, suspended length  $L = 500$  nm, and determine the misalignment angle  $\phi$  between applied magnetic field and the CNT axis. **c**, Band bending in the suspended CNT segment and neighbouring oxide-bound segments when  $V_g = V^*$ . The number of thermally activated carriers is minimized and there is no n-type region to facilitate tunnelling processes. The oxide-bound sections remain p-type at small  $V_g$ .

Table 1 Summary of thermal activation results

	$D$ (nm)	$E_g^0$ (meV)	$\phi$ (°)	$a$ (meV T <sup>-1</sup> )	$\mu_{orb}$ (meV T <sup>-1</sup> )	
					Experiment	Theory
Device 1	2.6 ± 0.3	36 ± 3	30 ± 3	1.3 ± 0.1	0.7 ± 0.1	0.5 ± 0.1
			60 ± 3	0.7 ± 0.1	0.7 ± 0.1	0.5 ± 0.1
Device 2	5.0 ± 0.3	40 ± 3	45 ± 3	2.1 ± 0.2	1.5 ± 0.2	1.0 ± 0.2

$\phi$  is the misalignment angle between CNT axis and the magnetic field direction. The experimental value of  $\mu_{orb}$  is given by  $a/2\cos\phi$ . There is uncertainty in theoretical values of  $\mu_{orb}$  owing to uncertainty in  $V_F$  and  $D$ .

CNTQD in device 1 at  $V_g > V^*$ ,  $T = 1.5$  K. There is a large region of zero conductance as the Fermi level passes through the energy gap of the suspended section. At higher  $V_g$  the Coulomb diamonds labelled 1, 2, 3 and 4 correspond to charge states of one, two, three and four electrons in the conduction band of the suspended segment.

In the Coulomb blockade model of quantum dots<sup>23</sup>, the width of the  $N$ th diamond is proportional to a fixed electrostatic charging energy plus the energy difference between the quantum levels occupied by  $N$ th and  $(N + 1)$ th electrons. The energies of the quantum levels in our CNTQD can be estimated by considering electrons confined to a 1D potential well of length  $L$ . The confinement results in quantized  $k_{||}$  values which, combined with the dispersion relations  $E_i(k_{||})$ , determine the energy levels of the dot. Near the bandgap edge  $E_i(k_{||})$  are parabolic, therefore, the energy levels of the first few conduction states should be:

$$\varepsilon(n, i, B_{||}) = \frac{E_g^0}{2} + \frac{\hbar^2 \pi^2}{2m_i^* L^2} n^2 \pm \mu_{orb} B_{||} \quad (3)$$

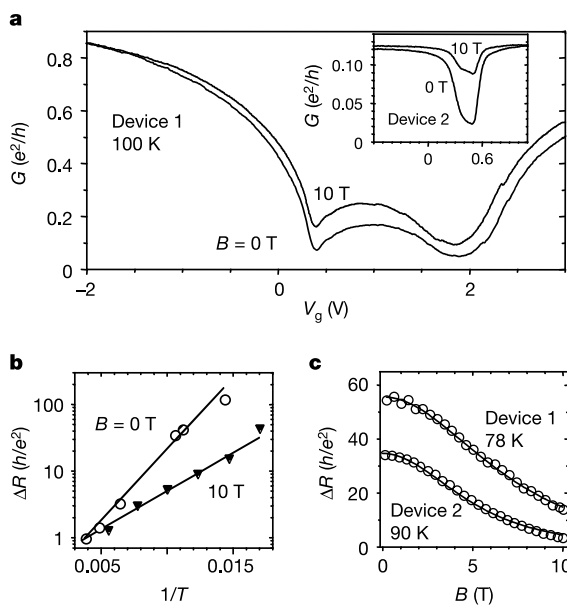
where the quantum number  $n$  is a positive integer, the effective mass  $m_i^* = E_g^{K_i}(B_{||})/2v_F^2$ , and + applies to CW orbitals while - applies to ACW orbitals. The first few level crossings predicted by equation (3) are shown in Fig. 4b.

Figure 4c shows low-bias  $G-V_g$  plots of a Coulomb peak from device 1 as  $B$  is increased. The peak corresponds to the second electron added to the dot (the intersection of Coulomb diamonds 1 and 2). The peak shifts  $\sim 1.2$  mV  $T^{-1}$  and doubles in conductance as  $B$  reaches 3.6 T. Figure 4d shows the first eight Coulomb peaks. The positions of the peaks generally move between 1.2 and 1.6 mV  $T^{-1}$ . The fifth and subsequent peaks show clear changes between positive and negative slopes. Peaks appear to be paired, each pair having a different zigzag pattern.

The main features of Fig. 4d are described by the CNTQD model. Peaks with  $d\varepsilon/dB > 0$  correspond to tunnelling into a CW orbital, while peaks with  $d\varepsilon/dB < 0$  correspond to tunnelling into a ACW orbital. The measured value of  $\mu_{orb} = |d\varepsilon/dB_{||}| = 0.7 \pm$

0.1 meV  $T^{-1}$  is inferred as described in the legend of Fig. 4, and agrees with the values in Table 1 for device 1. Furthermore, the striking difference between the first four peaks and later peaks is in qualitative agreement with the modelled spectrum (Fig. 4b). The first pair of peaks (spin up and spin down,  $n = 1$ , ACW orbital) are not expected to undergo level crossings. The second pair (peaks 3 and 4 in Fig. 4d) may undergo a level crossing at low field, but the resolution of our data is limited by thermal broadening; levels separated by less than  $4k_B T \approx 0.5$  meV merge together. The third and fourth pairs clearly show the changes in slope that are expected when level crossings occur. We conclude that there are quantum levels near the bandgap edges with both positive and negative orbital magnetic moments whose magnitudes are consistent with theoretical predictions<sup>4,5</sup>. The Coulomb blockade model does not describe all the features in Fig. 4d. The detailed structure of this CNTQD system may depend on effects such as exchange coupling<sup>21,24</sup>, and will be the subject of future work.

Our measured values of  $\mu_{orb}$  are 10–20 times larger than the Bohr



**Figure 3** Effect of magnetic field on device resistance. **a**,  $I-V_g$  curves for devices 1 and 2 at  $T = 100$  K. Curves taken at  $B = 0$  T have lower conductance than curves taken at  $B = 10$  T. **b**,  $\Delta R$  as a function of  $1/T$  for device 2. The data shown are for  $B = 0$  T (larger  $\Delta R$ ) and  $B = 10$  T (smaller  $\Delta R$ ). **c**,  $\Delta R$  as a function of  $B$  for device 1 at  $T = 78$  K (upper curve) and device 2 at  $T = 90$  K (lower curve).

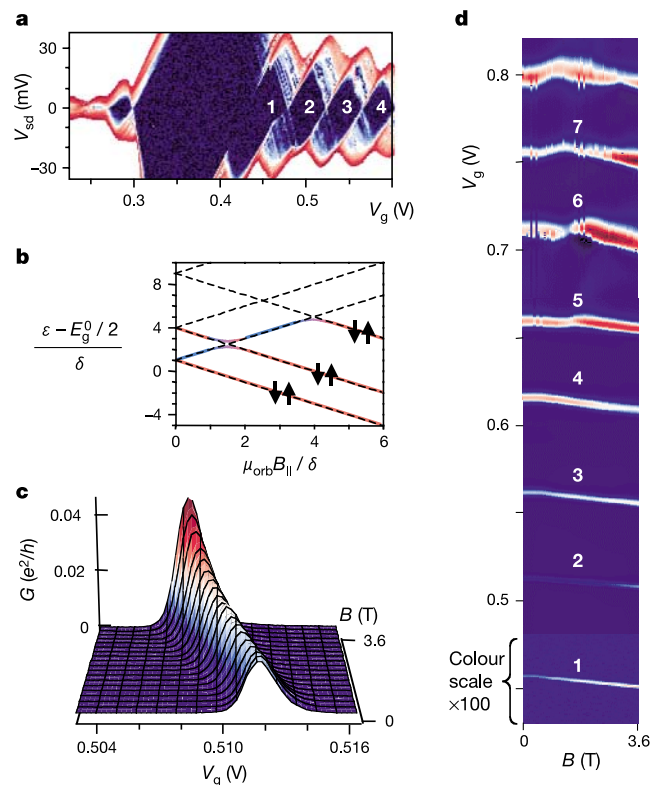


**Figure 4** Energy levels of a nanotube quantum dot. **a**, Differential conductance  $dI/dV_{sd}$  as a function of source-drain voltage,  $V_{sd}$ , and  $V_g$ . Data are from device 1 at  $T = 1.5$  K. Dark blue represents  $dI/dV_{sd} = 0$ , dark red represents  $dI/dV_{sd} = 0.2 e^2/h$ . In the white regions (top and bottom of the plot), current levels exceeded the measurement range. The first four Coulomb diamonds, corresponding to discrete charge states, are labelled 1–4. The gate coupling  $\alpha$  is twice the ratio of Coulomb diamond width to Coulomb diamond height<sup>23</sup>. For this device  $\alpha \approx 2.2$ . **b**, Modelled energies of quantum levels from equation (3), approximating  $m_i^*$  as constant. The energy scale  $\delta = \hbar^2 \pi^2 / 2m_i^* L^2$ . For device 1 we have  $\delta \approx 0.25$  meV. Coloured lines represent expected zigzags in the first six Coulomb peaks, with red and blue representing respectively ACW and CW states. Arrows indicate spin degeneracy for each state. **c**, Conductance  $I/V_{sd}$  as a function of magnetic field  $B$  for the second Coulomb peak of device 1,  $\phi = 30^\circ$ ,  $V_{sd} = 0.5$  mV. Shifts in peak position  $V_g^0(n, i)$  are related to energy shifts of quantum levels by:  $dV_g^0(n, i)/dB = \alpha d\varepsilon(n, i)/dB$ . **d**, Low-bias conductance  $I/V_{sd}$  as a function of  $V_g$  and  $B$  showing first eight Coulomb peaks of device 1,  $\phi = 30^\circ$ . Dark blue represents  $I/V_{sd} = 0$ ; dark red represents  $I/V_{sd} = 0.35 e^2/h$ . The colour scale for peak 1 is magnified by 100 times.

magneton and the spin magnetic moment in CNTs<sup>21,22</sup>. The reason is the large size of electron orbits encircling the CNT compared to the radii of atomic orbitals. These large magnetic moments give researchers a powerful new tool to control the energy structure of CNTs. For example, the tunnel transparency of p–n barriers can be tuned by using a magnetic field to modify the bandgap. This effect is seen in Fig. 4c: the conductance of the Coulomb peak increases as the tunnel barriers become more transparent. This will be useful, for example, to study Kondo physics in CNTQDs<sup>24,25</sup> at different tunnelling strengths. Researchers can also tune the energy levels of electrons in the 1D box formed by a CNT. By applying large magnetic fields it is possible to investigate the properties of a CNT in which only one sub-band is occupied. Conversely, by matching the energies of different sub-band states, the interactions between states arising from CW and ACW orbits can be explored. □

Received 18 December 2003; accepted 18 February 2004; doi:10.1038/nature02425.

1. Sohn, L. L., Kouwenhoven, L. P. & Schon, G. (eds) *Carbon Nanotubes* (Springer, New York, 2001).
2. Wildoer, J. W. G., Venema, L. C., Rinzler, A. G., Smalley, R. E. & Dekker, C. Electronic structure of atomically resolved carbon nanotubes. *Nature* **391**, 59–62 (1998).
3. Odom, T. W., Huang, J. L., Kim, P. & Lieber, C. M. Atomic structure and electronic properties of single-walled carbon nanotubes. *Nature* **391**, 62–64 (1998).
4. Ajiki, H. & Ando, T. Electronic states of carbon nanotubes. *J. Phys. Soc. Jpn* **62**, 1255–1266 (1993).
5. Lu, J. P. Novel magnetic-properties of carbon nanotubes. *Phys. Rev. Lett.* **74**, 1123–1126 (1995).
6. Ramirez, A. P. *et al.* Magnetic-susceptibility of molecular carbon—nanotubes and fullerite. *Science* **265**, 84–86 (1994).
7. Wang, X. K., Chang, R. P. H., Patashinski, A. & Ketterson, J. B. Magnetic-susceptibility of buckytubes. *J. Mater. Res.* **9**, 1578–1582 (1994).
8. Chauvet, O. *et al.* Magnetic anisotropies of aligned carbon nanotubes. *Phys. Rev. B* **52**, R6963–R6966 (1995).
9. Walters, D. A. *et al.* In-plane-aligned membranes of carbon nanotubes. *Chem. Phys. Lett.* **338**, 14–20 (2001).
10. Fujiwara, A., Tomiyama, K., Suematsu, H., Yumura, M. & Uchida, K. Quantum interference of electrons in multiwall carbon nanotubes. *Phys. Rev. B* **60**, 13492–13496 (1999).
11. Bachold, A. *et al.* Aharonov-Bohm oscillations in carbon nanotubes. *Nature* **397**, 673–675 (1999).
12. Lee, J. O. *et al.* Observation of magnetic-field-modulated energy gap in carbon nanotubes. *Solid State Commun.* **115**, 467–471 (2000).
13. Kane, C. L. & Mele, E. J. Size, shape, and low energy electronic structure of carbon nanotubes. *Phys. Rev. Lett.* **78**, 1932–1935 (1997).
14. Yang, L. & Han, J. Electronic structure of deformed carbon nanotubes. *Phys. Rev. Lett.* **85**, 154–157 (2000).
15. Minot, E. D. *et al.* Tuning carbon nanotube band gaps with strain. *Phys. Rev. Lett.* **90**, 156401 (2003).
16. Kwon, Y. K. & Tomanek, D. Electronic and structural properties of multiwall carbon nanotubes. *Phys. Rev. B* **58**, R16001–R16004 (1998).
17. Zhou, C. W., Kong, J. & Dai, H. J. Intrinsic electrical properties of individual single-walled carbon nanotubes with small band gaps. *Phys. Rev. Lett.* **84**, 5604–5607 (2000).
18. de Pablo, P. J. *et al.* Nonlinear resistance versus length in single-walled carbon nanotubes. *Phys. Rev. Lett.* **88**, 036804 (2002).
19. Yaish, Y. *et al.* Electrical nanoprobng of semiconducting carbon nanotubes using an atomic force microscope. *Phys. Rev. Lett.* **92**, 046401 (2004).
20. Maiti, A., Svizhenko, A. & Anantram, M. P. Electronic transport through carbon nanotubes: Effects of structural deformation and tube chirality. *Phys. Rev. Lett.* **88**, 126805 (2002).
21. Tans, S. J., Devoret, M. H., Groeneveld, R. J. A. & Dekker, C. Electron-electron correlations in carbon nanotubes. *Nature* **394**, 761–764 (1998).
22. Cobden, D. H., Bockrath, M., McEuen, P. L., Rinzler, A. G. & Smalley, R. E. Spin splitting and even-odd effects in carbon nanotubes. *Phys. Rev. Lett.* **81**, 681–684 (1998).
23. Sohn, L. L., Kouwenhoven, L. P. & Schon, G. (eds) *Mesoscopic Electron Transport* (Kluwer, Dordrecht, 1997).
24. Liang, W. J., Bockrath, M. & Park, H. Shell filling and exchange coupling in metallic single-walled carbon nanotubes. *Phys. Rev. Lett.* **88**, 126801 (2002).
25. Nygard, J., Cobden, D. H. & Lindelof, P. E. Kondo physics in carbon nanotubes. *Nature* **408**, 342–346 (2000).
26. Kong, J., Soh, H. T., Cassell, A. M., Quate, C. F. & Dai, H. J. Synthesis of individual single-walled carbon nanotubes on patterned silicon wafers. *Nature* **395**, 878–881 (1998).
27. Rosenblatt, S. *et al.* High performance electrolyte gated carbon nanotube transistors. *Nano Lett.* **2**, 869–872 (2002).

**Acknowledgements** We thank H. Ustunel, T. Arias and H. Dai for discussions. This work was supported by the NSF through the Cornell Center for Materials Research and the Center for Nanoscale Systems, and by the MARCO Focused Research Center on Materials, Structures, and Devices. Sample fabrication was performed at the Cornell node of the National Nanofabrication Users Network, funded by NSF. One of us (E.D.M.) acknowledges support by an NSF graduate fellowship.

**Competing interests statement** The authors declare that they have no competing financial interests.

**Correspondence** and requests for materials should be addressed to P.L.M. (mceuen@ccmr.cornell.edu).

## Current-induced domain-wall switching in a ferromagnetic semiconductor structure

M. Yamanouchi<sup>1</sup>, D. Chiba<sup>1</sup>, F. Matsukura<sup>1,2</sup> & H. Ohno<sup>1,2</sup>

<sup>1</sup>Laboratory for Nanoelectronics and Spintronics, Research Institute of Electrical Communication, Tohoku University, Katahira 2-1-1, Aoba-ku, Sendai 980-8577, Japan

<sup>2</sup>ERATO Semiconductor Spintronics Project, Japan Science and Technology Agency, Japan

Magnetic information storage relies on external magnetic fields to encode logical bits through magnetization reversal. But because the magnetic fields needed to operate ultradense storage devices are too high to generate, magnetization reversal by electrical currents is attracting much interest as a promising alternative encoding method. Indeed, spin-polarized currents can reverse the magnetization direction of nanometre-sized metallic structures through torque<sup>1–4</sup>; however, the high current densities of  $10^7$ – $10^8$  A cm<sup>–2</sup> that are at present required exceed the threshold values tolerated by the metal interconnects of integrated circuits<sup>5,6</sup>. Encoding magnetic information in metallic systems has also been achieved by manipulating the domain walls at the boundary between regions with different magnetization directions<sup>7–13</sup>, but the approach again requires high current densities of about  $10^7$  A cm<sup>–2</sup>. Here we demonstrate that, in a ferromagnetic semiconductor structure, magnetization reversal through domain-wall switching can be induced in the absence of a magnetic field using current pulses with densities below  $10^5$  A cm<sup>–2</sup>. The slow switching speed and low ferromagnetic transition temperature of our current system are impractical. But provided these problems can be addressed, magnetic reversal through electric pulses with reduced current densities could provide a route to magnetic information storage applications.

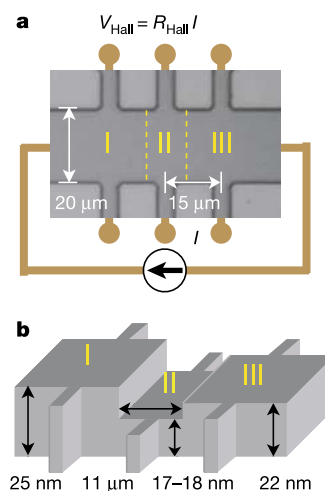


**Figure 1** A micrograph and a schematic drawing of the device. **a**, A 20- $\mu$ m-wide channel with three pairs of Hall probes separated by 15  $\mu$ m was defined by photolithography and wet etching. **b**, To reduce the coercive force of the two regions, 7–8 nm and 3 nm of the surface layers of regions II and III, respectively, were removed. A domain wall was prepared at the boundary of regions I and II, and its position after application of a current pulse was monitored by  $R_{\text{Hall}} = V_{\text{Hall}}/I$ , using a small probe current  $I$ . Hall voltage  $V_{\text{Hall}}$  is measured at the Hall probes. Magneto-optical Kerr microscopy was also used to image the domain structure.